

# Systematic Experimental Study on the Thermal Mixing Characteristics of Parallel Twin Water Jets Using UDV

Lingyun Zhang<sup>1,3</sup>, Songbai Cheng<sup>2,1,\*</sup>, Xiaolin Chen<sup>3</sup>, Xiaoxing Liu<sup>1</sup>

<sup>1</sup> Sino-French Institute of Nuclear Engineering & Technology, Sun Yat-Sen University, Zhuhai City, Guangdong Province 519082, China

<sup>2</sup> School of Nuclear Science and Technology, Harbin Engineering University, Harbin, Heilongjiang Province 150001, China

<sup>3</sup> Advanced Energy and Nuclear Technology Research Center, Advanced Energy Science and Technology Guangdong Laboratory, Huizhou City, Guangdong Province 516002, China

\* Corresponding author. E-mail: chengsongbai@hrbeu.edu.cn (S. Cheng).

## Abstract

To obtain a comprehensive understanding of the mechanisms underlying the thermal mixing phenomenon of coolant jet flowing from the core outlet in a Lead-cooled Fast Reactor (LFR), a systematic research project has been initiated recently under the collaboration between the Sun Yat-sen University and Harbin Engineering University in China. In the first stage of the project, experiments were conducted in the Thermal-hydraulic characteristics in Liquid Jet Mixing (TLJM) apparatus. Parallel twin water jets under various thermal and hydraulic conditions were mixed in a rectangular water pool and the mixing behavior was measured by using the Ultrasonic Doppler Velocimetry (UDV). The study analyzed the transient characteristics of water jets in the thermal mixing zone, including flow velocity, temperature as well as their fluctuation intensity distributions. Additionally, the impact of experimental parameters (e.g. inlet velocity, temperature, velocity ratio, and hydraulic diameter) on the velocity field, temperature field, and their fluctuation intensity distributions were also examined in detail. The results indicate that thermal mixing occurs in specific regions and follows distinct patterns with main fluctuation frequencies up to 10 Hz. Velocity fluctuations are tightly coupled with temperature fluctuations, as turbulence enhances thermal diffusion in the mixing zone. All experimental parameters are found to have noticeable influence on the mixing patterns. The study provides valuable insights and database on the thermal mixing mechanism and also verifies the applicability of UDV in transient velocity measurement. The obtained knowledge benefits the upcoming lead-bismuth experiments and ultimately contributes to future design and safety analysis of LFRs.

**Keywords:** Lead-cooled Fast Reactor; Parallel jets; Thermal mixing; Water jet mixing characteristics

## 1. Introduction

In recent years, Sodium-cooled Fast Reactors (SFRs) and Lead-cooled Fast Reactors (LFRs) have been accepted as promising GEN-IV nuclear systems. In these

Liquid Metal-cooled Fast Reactors (LMFRs), liquid metal coolant flows out from the core outlet with different temperatures due to the non-uniform core power distribution. In the upper plenum, cold and hot coolant flows mix in the form of jets and plumes. The inadequate mixing could lead to the temperature fluctuations which would be transmitted to the adjacent solid structures through convective heat transfer. This phenomenon first observed in the 1970s was called thermal striping in LMFRs [1-3]. The thermal striping may cause thermal fatigue in structural components and eventually may lead to structural damage or failure that threatens the safety of reactors [4,5]. Therefore, understanding the flow mixing mechanisms and accurately predicting the thermal striping characteristics of liquid metal coolant, are crucial for the design and operation of LMFRs.

Previous researchers have conducted many experiments to investigate the flow mixing behaviour at core outlet. Due to the complexity of the structure at core outlet region, simplified models like parallel jets and coaxial jets were taken into account. The experimental studies on the mixing of different working fluids in different models are summarized in Table 1. Moriya and Ohshima [6] measured the temperature in coaxial jets mixing using sodium, water, and air, and found that, if the Reynolds and Peclet numbers are significantly large, the temperature fluctuation characteristics of sodium can be evaluated by experiments using water or air. Tenchine and Moro [7] studied the mixing of coaxial vertical jets using sodium and air. They indicated that the temperature fluctuations of air and sodium agree well when the Reynolds number of the air was sufficiently high. Ahmed and Sharma [8] investigated the turbulent mixing of confined coaxial air jets, suggesting that mixing process depends on the velocity ratio as well as the interaction between the boundary layer, mixing layer and the main flow. Wakamatsu et al. [9] analyzed the attenuation of temperature fluctuations from parallel impinging jets to the structure surface using sodium and water. They obtained the attenuation ratios of temperature fluctuations in water tests and sodium tests separately. Tokuhio and Kimura [10] investigated the thermal-hydraulic mixing of triple water jets and described the characteristics of the convective mixing region between jets by estimating the turbulent heat flux. In a parallel triple sodium jets experiment, Kimura et al. [11] evaluated the transfer characteristics of temperature fluctuations from fluid to structures and proposed a method to evaluate the heat transfer coefficients. Lu et al. [12] revealed the 3D characteristics of the transient temperature fluctuations caused by the coaxial water jets flow. Cao et al. [13] observed an axisymmetric distribution of time-averaged temperatures when the velocity ratio of the coaxial water jets flow was over 1, and verified that the region and the intensity of temperature fluctuations are different from those with velocity ratio equal to 1. Kok et al. [14] obtained the dominant frequency of temperature fluctuation as 5 Hz in a coaxial water jets experiment. They found that the thermal mixing efficiency was enhanced with increasing temperature difference between jets. In their subsequent mixing experiment of parallel twin water jets [15], they concluded that the sequential obstacles increase the thermal mixing efficiency. Although more detailed data and characteristics of the thermal mixing would be preferable, it is evident that the above experimental investigations can provide a

benchmark database for the validation and verification of numerical simulation.

Table 1 Experimental studies on the thermal mixing of different working fluids.

Author	Working fluid	Model of jets
Moriya and Ohshima [6]	sodium, water, air	coaxial jets
Tenchine and Moro [7]	sodium, air	coaxial vertical jets
Ahmed and Sharma [8]	air	confined coaxial jets
Wakamatsu et al. [9]	sodium, water	parallel impinging jets
Tokuhiro and Kimura [10]	water	parallel triple jets
Kimura et al. [11]	sodium	parallel triple jets
Lu et al. [12]	water	coaxial jets
Cao et al. [13]	water	coaxial jets
Kok et al. [14]	water	coaxial jets
Kok et al. [15]	water	parallel twin jets

The Computational Fluid Dynamics (CFD) simulation has been widely applied in the thermal-hydraulics design and analysis of LMFs in recently years [16]. Yu et al. [17] applied Reynolds-Average Navier-Stokes (RANS) and Unsteady Reynolds-Average Navier-Stokes (URANS) methods in the simulation of parallel triple sodium jets mixing, and found that RANS models are unable to accurately predict the temperature fluctuations. Large Eddy Simulation (LES) has been considered as a promising approach to describe the instantaneous temperature fluctuations since most of the eddies are computed instead of being modeled. For this reason, LES method is applied in the benchmark simulation of jets mixing experiments [14,15,17,18,19, 20] and also in the simulation of jets mixing at realistic core outlet [21, 22, 23].

Due to the property of low Prandtl number, the thermal mixing behavior of liquid metal shows significant difference compared with that of water or air. To the author's knowledge, there is no experiment on the thermal mixing of lead or lead-based alloy jets so far. The similarity criteria obtained in water or air experiments [6,7] to predict sodium temperature fluctuations may not be directly applied in LFRs. Additionally, the Particle Image Velocimetry (PIV) employed in previous water experiments can not be applied to the opaque fluid, which means that a reliable method or technique for the velocity measurement in liquid metal is necessary. Therefore, more effort, including the improvement of instruments, is needed to investigate the thermal mixing of liquid lead or lead-based alloy in LFRs.

Motivated by achieving a more comprehensive understanding on the thermal mixing mechanism of liquid lead-bismuth and then accurately predicting the thermal mixing phenomenon in LFRs, a systematic research project that consists of three well-organized stages, has been launched under the collaboration between the Sun Yat-sen University and Harbin Engineering University. In the first stage, an experimental apparatus is established to study the mixing of parallel twin jets using water, employing Ultrasonic Doppler Velocimetry (UDV) for velocity measurement to verify its applicability and performance. In parallel, numerical simulation using LES

method is also performed for the validation against experimental data. The data which is more comprehensive than experiments, is expected for the in-depth analysis of the thermal mixing phenomenon. In the second stage, a lead-bismuth test loop would be established, in which thermal mixing experiments of lead-bismuth jets will be carried out. The validation and verification of LES numerical simulation are also expected to obtain a better understanding on the thermal mixing characteristics of liquid lead-bismuth. In the third stage, numerical simulation of the thermal mixing characteristics of the jets from core outlet of a realistic LFR model and conditions will be performed. The results and data would provide important values and evidence for the future industrial design and improvement of LFRs.

This paper focuses on the experimental activities in the first stage of the project. A series of water experiments in the parallel twin jets flow were performed under various inlet conditions. Velocity and temperature fluctuations in the mixing zone were measured and analyzed. The knowledge and favorable experimental data obtained from this study will be soon employed for the validation of numerical simulation and then provide reference and guidance for the liquid lead-bismuth experiments in the following stage of the project.

## 2. Experimental study

### 2.1. Facility description

The experimental facility consists of loop system and test section. The loop system contains the cold fluid loop and the hot fluid loop. In each loop the water in storage tank is heated to the desired temperature by a heating rod. Then the pumps are activated and drive the fluid at controlled flow rates. The cold water and hot water flow into a jet generator and then is injected into the test section. After mixing in test section, the water flows back to water tanks via the drains. The schematic of the loop system including connecting piping, flowmeters and valves is given in Fig. 1.

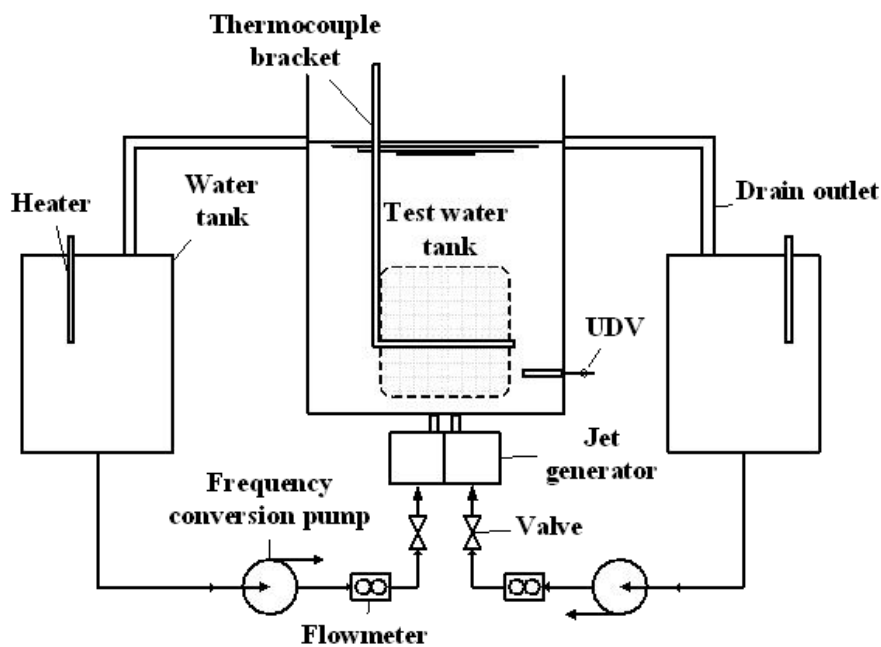


Fig. 1. Schematic of the experimental loop system.

The test section is a rectangular transparent water tank with the length of 400 mm, the width of 60 mm and the height of 800 mm, as shown in Fig. 2. Two rectangular injection nozzles are set parallel at the central bottom of the test section without level difference. The nozzles have the same length as the width of test section (see Fig. 2), while their widths can be adjusted to a variety of sizes. The cold fluid and hot fluid are injected through the nozzles, mix in the form of parallel twin jets and then flow out of the test section through the drain piping at the top. The Cartesian coordinate is adopted to analyze the flow velocity and temperature distribution in the mixing zone. As shown in Fig. 2, the  $x$ -axis is defined as the  $x$ -axis direction along the length, the  $z$ -axis as the vertical direction and the  $y$ -axis as the direction along the test section width. The origin of the coordinates is set at the center of the bottom of test section.

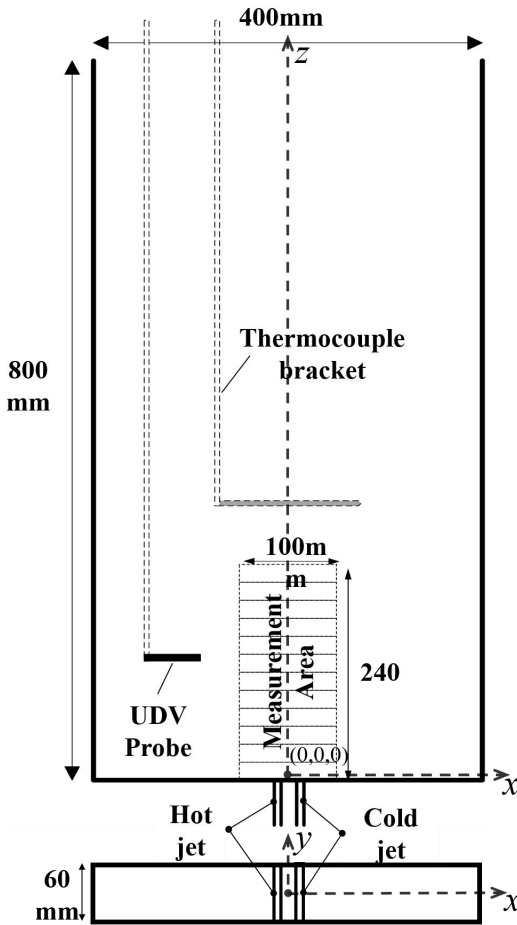


Fig. 2. Schematic of the test section.

## 2.2. Experimental measurements

The velocity field of the mixing zone in the test section is measured using UDV. Based on the Doppler effect, UDV measures the velocity of a fluid by emitting ultrasonic signals and receiving the reflected signal of the tracer particles inside the fluid. UDV can provide detailed information on the fluid velocity field without interfering with the fluid. The UDV DOP5000, which was manufactured by Signal Processing SA, is used in this study. In the measurement process, an appropriate

amount of tracer particles with a density close to water are added to ensure the intensity and effectiveness of the echo signal. The position of the UDV probe in the test section is shown in Fig 2, primarily measuring the velocity component of the  $x$ -axis to derive the turbulence distribution and frequency of fluctuations in the mixing zone.

The temperature in mixing zone is measured by a thermocouple system arranged as shown in Fig. 3. The K-type armored thermocouples are chosen, with the outer diameter of 1 mm and the measurement accuracy of  $\pm 0.4\%$ . The integrated frequency of signal acquisition can reach 64 Hz. Twenty thermocouple probes are arranged at intervals of 5 mm on the support which is movable in vertical direction.

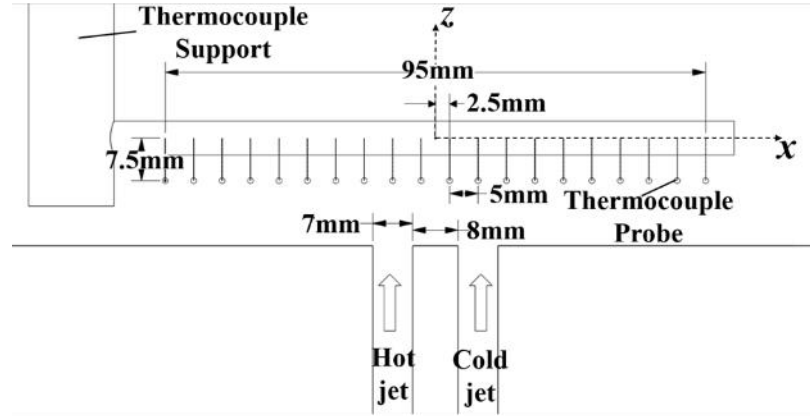


Fig. 3. Schematic of thermocouples arrangement

### 2.3. Inlet conditions and data processing method

The inlets conditions of the parallel twin water jets in experiments are given in Table 2. The temperature of cold water jet is set as 35°C while the temperature difference between hot jet and cold jet varies from 10 to 20 °C. The experiments include the cases of injection velocity ratios( $R$ ) from 0.5 to 2 and inlet hydraulic diameters( $D^*$ ) from 5.71 mm to 18.59 mm.

Table 2 Inlet conditions of jets in experiments.

	Cold jet		Hot jet		Temperature difference $\Delta T$ (K)	Velocity ratio $R$ (-)	Hydraulic diameter $D^*$ (mm)
	Temperature $T_c$ (°C)	Velocity $v_c$ (m/s)	Temperature $T_h$ (°C)	Velocity $v_h$ (m/s)			
Case1	35	0.5	45	0.5	10	1	12.54
Case2	35	1	45	1	10	1	12.54
Case3	35	1.5	45	1.5	10	1	12.54
Case4	35	0.5	50	0.5	15	1	12.54
Case5	35	1.5	55	1.5	20	1	12.54
Case6	35	0.5	55	0.5	20	1	12.54
Case7	35	0.5	45	1	10	0.5	12.54
Case8	35	1	45	0.5	10	2	12.54
Case9	35	0.5	45	0.5	10	1	18.59

Case10	35	0.5	45	0.5	10	1	5.71
--------	----	-----	----	-----	----	---	------

In the data processing, to better compare the temperature fluctuations in different cases, the normalized temperature  $T^*$  is defined as:

$$T^* = \frac{T - T_c}{\Delta T} \quad (1)$$

Where  $T$  is the measured temperature,  $T_c$  the temperature of cold fluid and  $\Delta T$  the temperature difference between cold fluid and hot fluid. The average temperature  $\bar{T}$

and its normalized value  $\bar{T}^*$  are expressed with:

$$\bar{T} = \frac{1}{N} \sum_i^N T_i \quad (2)$$

where  $N$  is the number of measurements within a certain time period.

$$\bar{T}^* = \frac{\bar{T} - T_c}{\Delta T} \quad (3)$$

The normalized value of root-mean-square (RMS) temperature  $T_{\text{RMS}}^*$  is defined to describe to intensity of the temperature fluctuations:

$$T_{\text{RMS}}^* = \sqrt{\frac{1}{N} \sum_i^N (T^* - \bar{T}^*)^2} \quad (4)$$

The normalized amplitude and frequency of the temperature fluctuations are obtained by the Fast Fourier Transform (FFT).

The non-dimensionless distance  $x^*$  and  $z^*$  are defined as follow:

$$x^* = x / D^* \quad (5)$$

$$z^* = z / D^* \quad (6)$$

where  $D^*$  is the inlet hydraulic diameter of the jets. The intensity of the velocity fluctuation in the  $x$ -axis at a certain position is defined by a standard deviation as:

$$\sigma_x = \sqrt{\frac{\sum_i^N (v_{x,i} - \bar{v}_x)^2}{N}} \quad (7)$$

where  $v_{x,i}$  is the measured transient velocity component in the  $x$ -axis in the time period,  $\bar{v}_x$  is the average of the  $v_{x,i}$ :

$$\bar{v}_x = \frac{1}{N} \sum_i^N v_{x,i} \quad (8)$$

### 3. Results and discussion

### 3.1. Flow field analysis

The thermal mixing process between hot and cold jets, as illustrated in Fig. 4, under Case 1 boundary conditions, effectively showcases the interaction of these flows. The employment of colorants as visualization agents permits clear observation of the jet mixing phenomenon without any modification to the physical properties of the working fluid (i.e. water in this case). The figures display a sequence of images taken at specific time intervals (0 s, 0.2 s, 0.4 s, 0.6 s, 0.8 s, and 1.0 s) using a high-speed camera, offering a dynamic view of the evolving mixing region. The figure clearly illustrates that the zone of thermal commingling is largely circumscribed within a defined rectangular volume, extending 250 millimeters vertically and 100 millimeters laterally. This volume, distinguished as the "Main Thermal Mixing Area" in the figure, is of paramount importance for the empirical measurement collection. Given that the  $D^*$  value for Case 1 is 12.54, the spatial dimensions of the critical region are presented in normalized form, with the  $x$ -axis spanning from -4.0 to 4.0 ( $x^*$ ) and the  $z$ -axis ranging from approximately 0 to 20 ( $z^*$ ). These specifications establish a standardized framework for evaluating the thermal mixing behavior observed in the experiment.

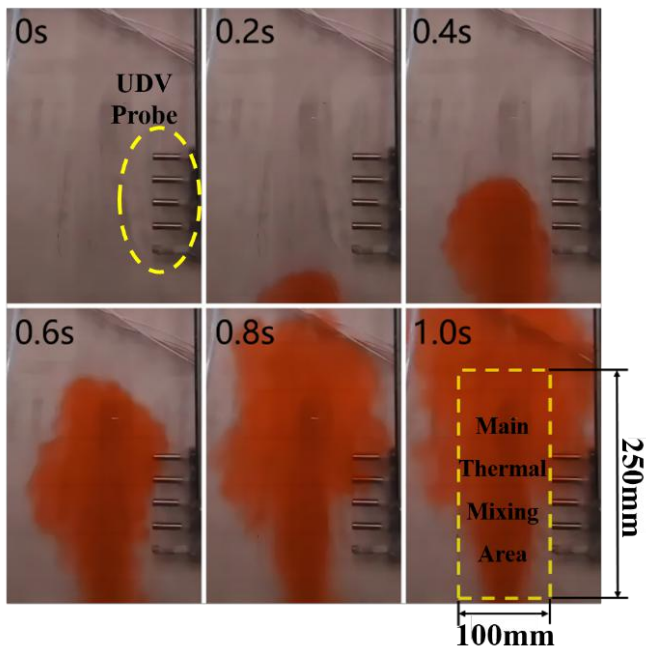


Fig. 4. Schematic diagram of capturing transient flow field

Fig. 5 presents a series of time-domain plots that capture the fluctuating nature of the instantaneous velocity component along the  $x$ -axis at four specific locations ( $x^* = -3, -1, 1, 3$ ), recorded at various vertical levels throughout a contiguous 3-second interval. These plots reflect the stable phase of the jet mixing process under the defined boundary conditions in Case 1. The plots delineate the velocity component's directional variability, with positive and negative values denoting movement in the respective positive and negative  $x$ -directions. It is striking to note that Fig. 5 reveals

the velocity component's amplitude range spans approximately from -0.15 m/s to 0.15 m/s. The figure also highlights a significant degree of variability in velocity direction across the different  $x$  positions, which is compelling evidence of intense and chaotic turbulent activity. This observation is suggestive of a potential recirculation phenomenon occurring within the mixing zone, underscoring the complex fluid dynamics in effect.

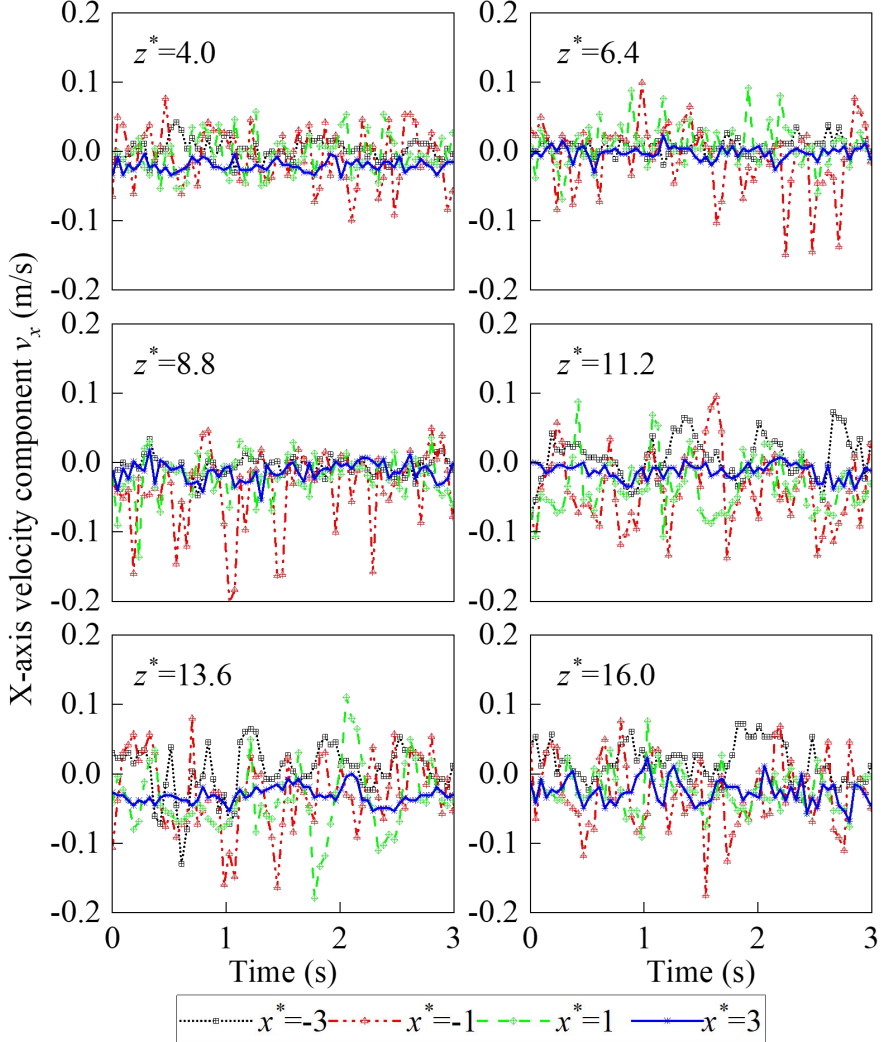


Fig. 5. Time-domain plot of transient  $x$ -axis velocity component

While the time-domain plot of the  $x$ -axis velocity component offers valuable insights, it falls short of providing a comprehensive depiction of the velocity field within the mixing zone. To address this limitation, we conducted a further examination of the velocity component along the  $z$ -axis. Fig. 6 portrays the transient velocity components in the  $z$ -axis at various vertical positions throughout a selected 1-second period during the stable mixing phase of Case 1. Here, positive transient velocity values denote the movement in the positive  $z$ -axis. The figure primarily illustrates an upward velocity direction, aligned with the jet's initial trajectory, with only isolated occurrences of local backflow manifesting as velocity values contrary to the jet's direction. A scrutiny of the velocities at the four distinct points along the

$x$ -axis reveals an intriguing dynamic: with the ascent of height ( $z^*$ ), both the breadth of the main flow region and the intensity of velocity oscillations exhibit a tendency to rise initially, followed by a subsequent decrease, thereby characterizing the complex interplay between flow dynamics within the mixing zone.

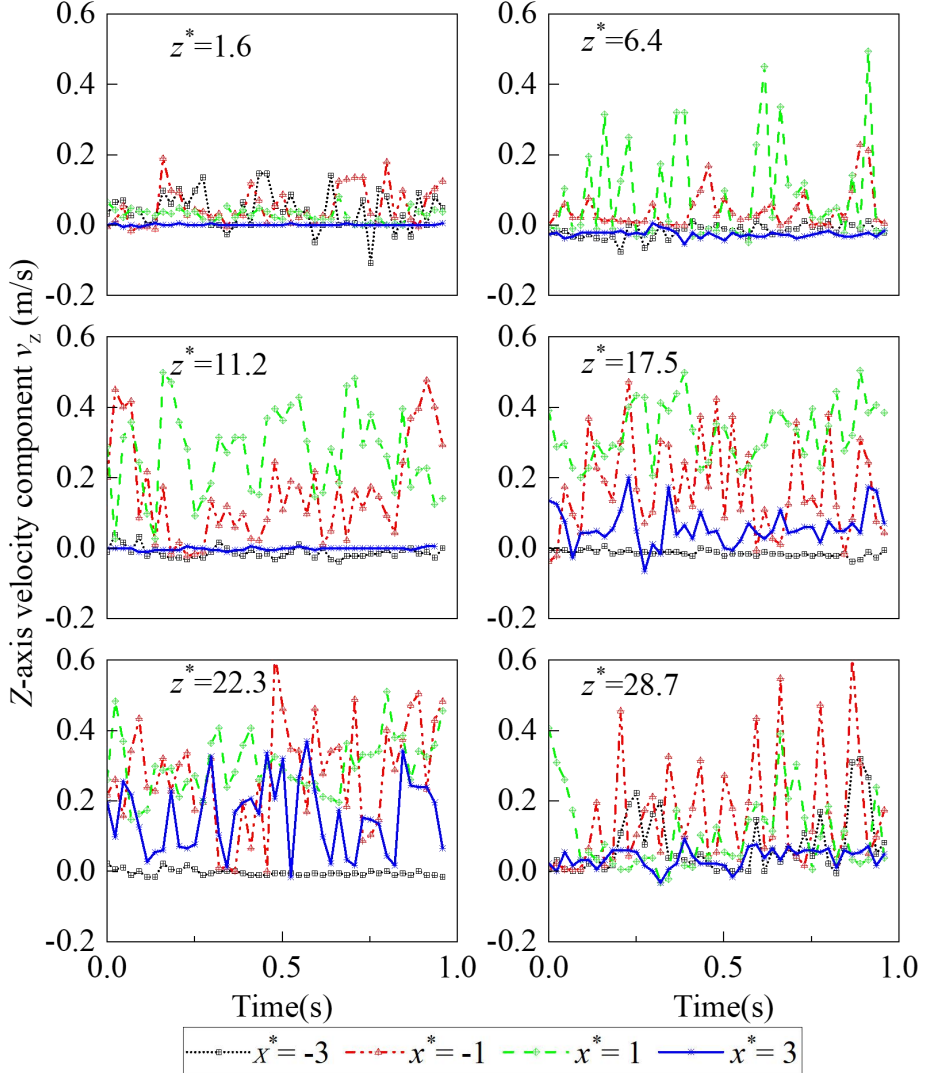


Fig. 6. Time-domain plot of transient  $z$ -axis velocity component

The evidence presented in Figs. 5 and 6 permits a nuanced characterization of the transient flow field associated with the thermal mixing of parallel twin jets. It is apparent that the mingling of the twin jets is largely localized to a defined area, remotely positioned from the jet inlets. In the vertical plane of development, the main flow exhibits not only an upward progression but also an inherent lateral instability, manifesting as an  $x$ -axis left-right oscillation. This dynamic behavior underscores the complex three-dimensional nature of the flow interactions within the mixing zone of twin jets.

The jet mixing process is a perpetual continuum, inherently marked by the presence of turbulence. While the depicted transient flow field diagram affords a qualitative appreciation of the flow dynamics within the mixing zone, a deeper,

quantitative understanding necessitates a more rigorous examination. To ascertain the magnitude and characteristics of velocity pulsations at various points within the flow field, and to elucidate the internal mechanisms that govern these dynamics, a thorough analysis of velocity statistics is indispensable. This involves the meticulous assessment of mean velocity values and the standard deviation, which together provide a more profound insight into the complex nature of the flow behavior.

Fig. 7(a) illustrates the distribution of the average and extreme values of 128 experimentally collected data points over a randomly selected two-second interval during the stable mixing phase of average velocity along the  $z$ -axis. Fig. 7(b) presents the corresponding measurement of the standard deviation for the dataset. An analysis of these data reveals that the velocity oscillations at various transverse positions and ascending through different stratifications, in the wake of the twin jets' intersection, evince a distribution that is nearly bilateral, indicating a commensurate extent of extremity between the left and right velocity components. Furthermore, the mean velocity on the  $x$ -axis is seen to remain in stasis, marginally above or below zero, throughout the interval under scrutiny. It is thus inferred that the mixing zone is imbued with a turbulent flow of disorder, engendering a multitude of directional changes within the flow field's velocity vector. When the jets are imbued with equal initial impact velocities of 0.5 m/s, the lateral velocity deviations are constrained to a modest figure of less than 0.25 m/s, highlighting the nuanced interplay of forces within the flow. Fig. 7(b) illustrates that the standard deviation (Std. Dev.) of the  $x$ -axis velocity components in the mixing zone generally exhibits a symmetric distribution, indicating a uniform turbulence mixing intensity on both sides. As  $z^*$  increases, the width of the region with higher standard deviation values in the  $x$ -axis expands significantly near the jet inlet ( $z$ -axis), though the turbulence mixing zone does not widen continuously with  $z^*$ .

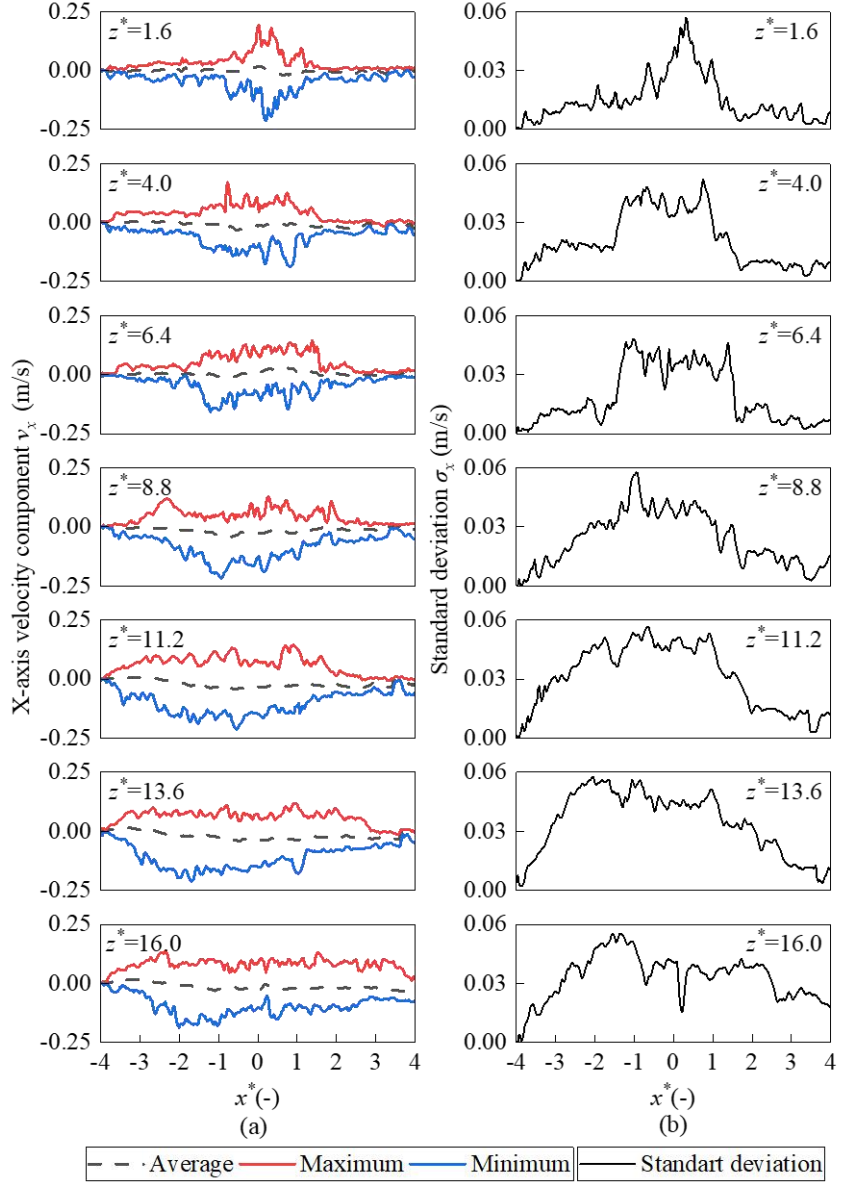


Fig. 7. Distribution of mean, extremes, and standard deviation of  $x$ -axis velocity field

The insights previously presented are based on empirical data collected under the parameters of Case 1, as tabulated in Table 2. Starting from Case 1, we systematically undertook a series of experiments, rigorously maintaining the principle of control variables. Within this framework, each experiment was carefully designed to modify just one parameter—either temperature, velocity, velocity ratio, or inlet hydraulic diameter—while holding all other factors constant, thereby enabling a nuanced observation of the effects of this parameter's fluctuation on the experimental results. The overarching aim of this methodological approach was to systematically explore and elucidate the influence of these various factors on the nuanced characteristics of the jet mixing distribution, thereby enhancing our understanding of the underlying fluid dynamics.

Fig. 8 depicts a comparison of the Std. Dev. of  $x$ -axis velocity components across varying initial velocities, considering scenarios where the cold and hot flow velocities

are equivalent. The Std. Dev. of the  $x$ -axis velocity components in the mixing zone typically exhibits a symmetric distribution, indicating uniform turbulence mixing intensity on both sides. As the inlet velocity increases, the overall Std. Dev. escalates, suggesting an intensification of turbulence mixing in the  $x$ -axis direction of the flow field in response to higher jet inlet velocities. At inlet velocities of  $v_c=v_h=0.5$  m/s and  $v_c=v_h=1.0$  m/s, the strongest velocity fluctuations near the centerline ( $x^*\approx 0$ ) are observed at  $z^*>19$ , such as at  $z^*=19.9$  and  $z^*=22.3$ . However, at  $v_c=v_h=1.5$  m/s, the strongest velocity fluctuation shifts significantly to  $z^*=11.2$ . This suggests that higher initial inlet velocities may lower the vertical extent of the thermal mixing region, leading to earlier completion of mixing. Furthermore, from the perspective of the  $x$ -axis gradient of velocity fluctuation intensity, regions with greater velocity fluctuations under all three inlet velocity conditions are primarily concentrated within the range of  $-2 < x^* < 2$ .

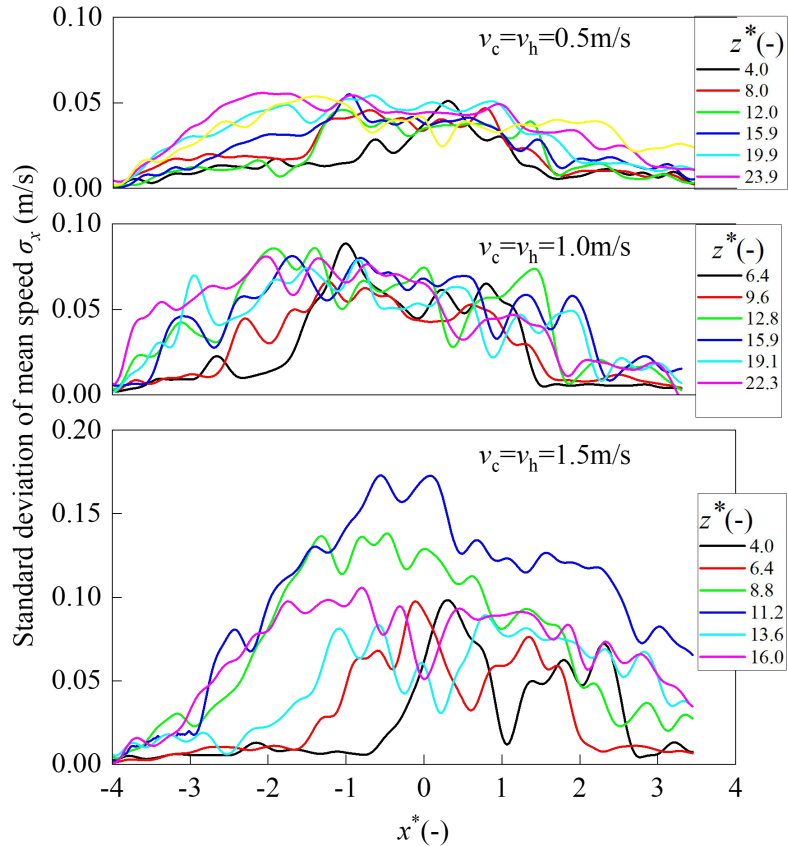


Fig. 8. Standard deviation comparison of  $x$ -axis velocity components across varying initial velocities ( $v_c=v_h$ )

Fig. 9 presents a comparative analysis of the Std. Dev. of  $x$ -axis velocity components within the thermal mixing zone for temperature differences of 10 K and 20 K. Initial observations reveal that the distribution form of the Std. Dev. for both  $\Delta T = 10$  K and  $\Delta T = 20$  K are strikingly similar. As the inlet jet temperature difference increases from 10 K to 20 K, a pronounced increase in the peak values of the Std. Dev. of  $x$ -axis velocity is evident at central positions within the thermal mixing zone,

specifically at  $z^*=2.8$  and  $z^*=6.8$ . This trend suggests that a higher temperature differential induces enhanced  $x$ -axis velocity fluctuations, which may facilitate the earlier onset of vigorous turbulent mixing. Notably, beyond  $z^* \geq 10.8$ , the reduction in the peak Std. Dev. of  $x$ -axis velocity observed for the larger temperature difference indicates that the mixing process is essentially complete. Regardless of the temperature difference ( $\Delta T = 10$  K or  $\Delta T = 20$  K), the velocity fluctuation intensity before the completion of mixing ( $z^* < 8.8$  in Fig. 9(a) and  $z^* < 6.8$  in Fig. 9(b)) exhibits a clear left-right symmetry at  $x$ -axis. However, after the completion of mixing, the velocity fluctuation distribution becomes asymmetric, particularly under larger temperature differences. For instance, in Fig. 9(b), the intensity difference between the two sides at  $z^*=14.8$  and  $z^*=16.7$  is more pronounced than that observed in Fig. 9(a) at  $z^*=13.6$  and  $z^*=16.0$ . This indicates that higher temperature differences amplify the asymmetry in velocity fluctuations after mixing is complete.

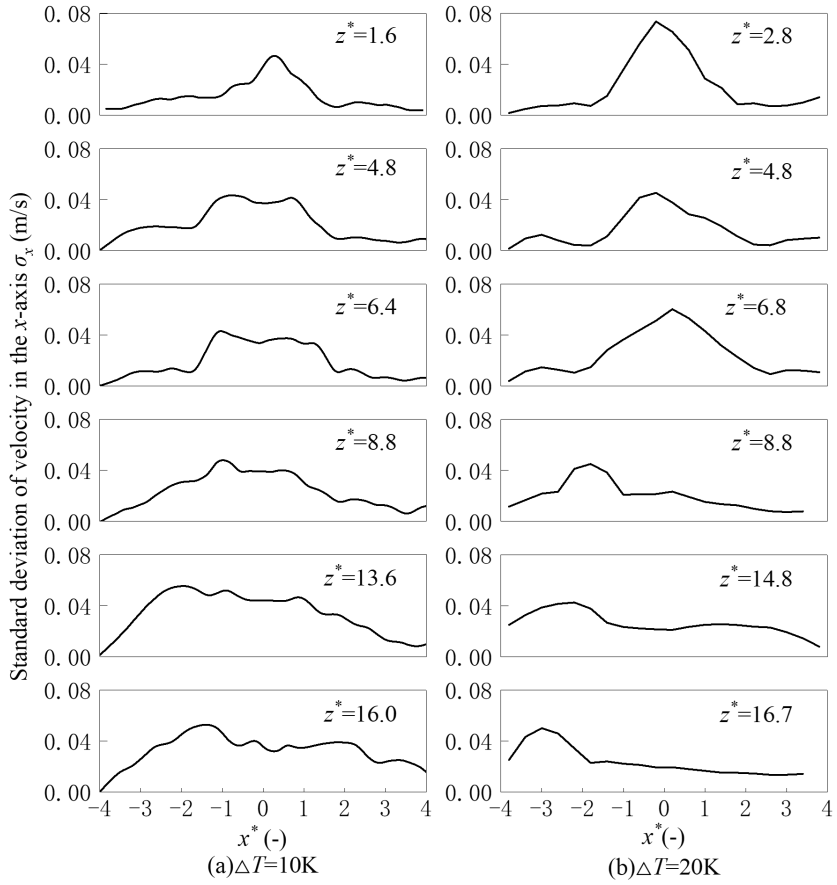


Fig. 9. Standard deviation of  $x$ -axis velocity components across varying inlet temperature differences

Fig. 10 provides the standard deviation (Std. Dev.) of the  $x$ -axis velocity component under the different velocity ratios. Across all cases, the Std. Dev. first increases and then decreases as  $z^*$  rises. Under  $R = 0.5$ , the velocity pulsation intensity is significantly higher on the hot jet side, while on the cold jet side ( $x^* > 1$ ), the pulsation intensity is almost negligible. Conversely, under  $R = 2$ , the pulsation intensity shifts to the cold jet side. The peak values of Std. Dev. are also

influenced by the velocity ratio: when  $R = 0.5$ , the peak ranges between 0.08 and 0.1 m/s, while for  $R = 2$ , it stabilizes between 0.06 and 0.08 m/s. This discrepancy arises from the stronger momentum of the hot jet under  $R = 0.5$ , resulting in more intense turbulent mixing.

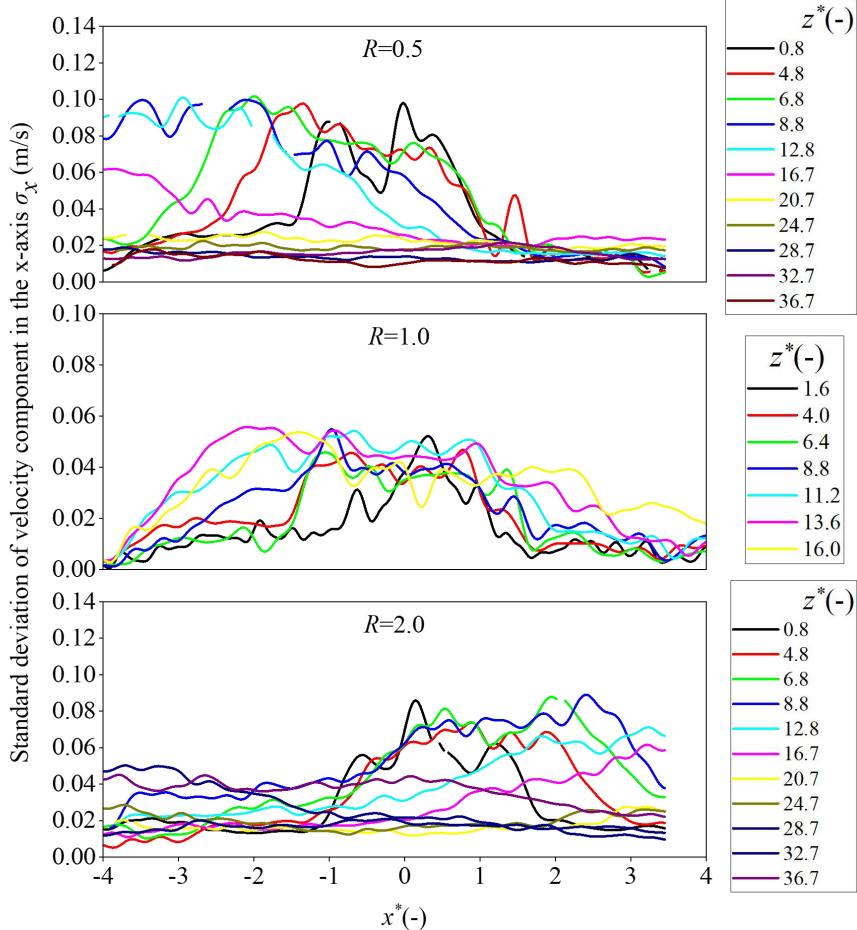


Fig. 10. Standard deviation of the  $x$ -axis velocity component under different velocity ratios

Fig. 11 illustrates the distribution of the Std. Dev. of  $x$ -axis velocity within the thermal mixing zone for three different inlet hydraulic diameters:  $D^* = 5.71$ ,  $12.54$ , and  $18.59$ . The figure shows that as the hydraulic diameter increases, the peak Std. Dev. of  $x$ -axis velocity also increases, which indicates a more intense turbulent mixing effect. For the smallest hydraulic diameter ( $D^* = 5.71$ ), the velocity fluctuations are relatively less intense and are distributed over a wider downstream region. At the same time, the Std. Dev. of  $x$ -axis velocity peak at a higher axial location (further from the inlet) suggests slower mixing process, indicative of reduced mixing efficiency. As the hydraulic diameter increases to  $D^* = 12.54$  or  $18.59$ , there is a noticeable increase in the intensity of the velocity fluctuations, with the peak Std. Dev. shifting closer to the inlet region. This indicates that the larger hydraulic diameter generates more intense turbulence, leading to faster and more localized mixing in the thermal zone. The more intense velocity fluctuations in this region likely enhance the heat exchange process, promoting more effective thermal mixing.

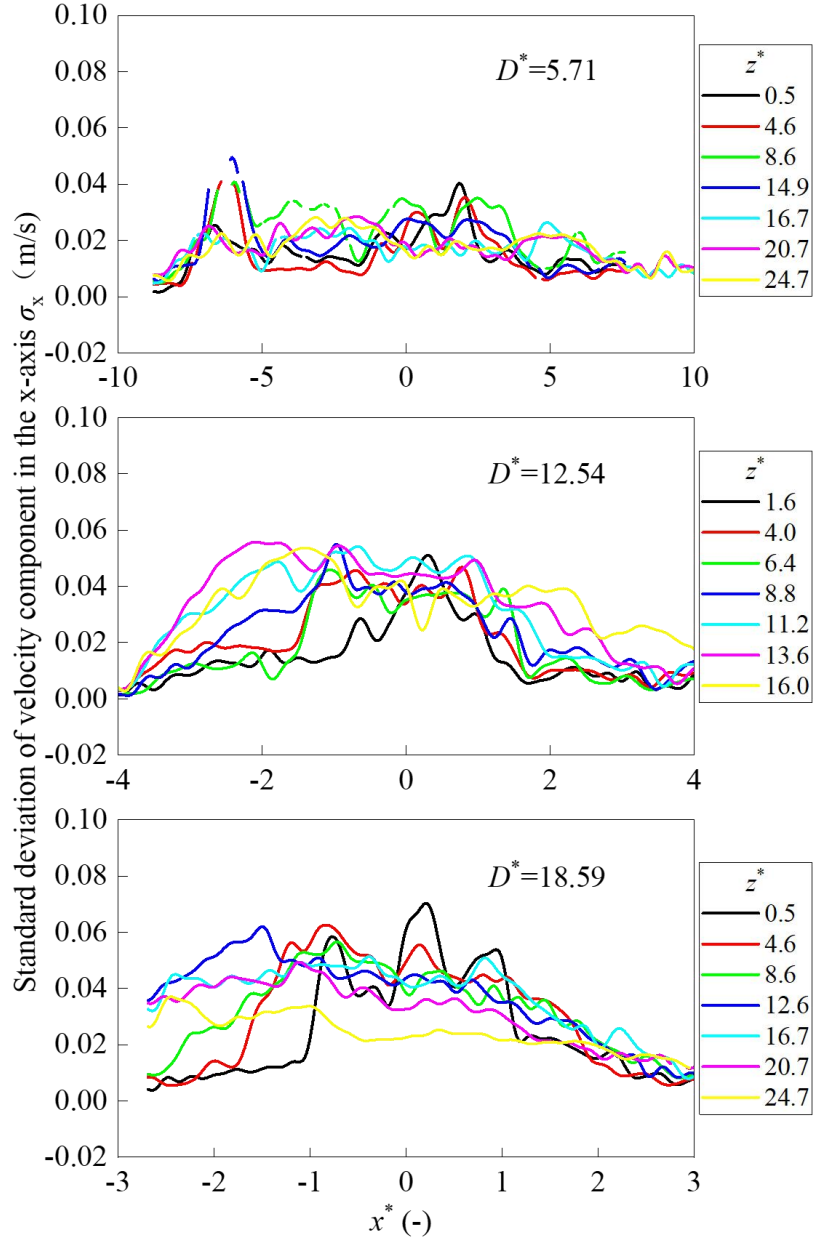


Fig. 11. Standard deviation of the  $x$ -axis velocity component under different inlet hydraulic diameters

### 3.2. Temperature field analysis

Fig. 12 elaborates on the intricate distribution of temperature fluctuations of Case 1 across various positions along the  $x$ -axis, at a pivotal  $z^* = 6.4$ , where substantial velocity fluctuations are discernible, as shown in Fig. 5. Specifically, Fig. 12(a) unveils the temporal evolution of the normalized temperature  $T^*$  in the time domain, while Fig. 12(b) meticulously portrays the amplitude ( $A^*$ ) of normalized RMS temperature ( $T^*_{\text{RMS}}$ ) as a function of frequency, derived via FFT analysis over the measurement interval. In terms of time-domain characteristics, the images reveal that temperature fluctuations exhibit distinct amplitudes and patterns at varying positions along the  $x$ -axis. Notably, positions within the range of  $x^*$  from -1.8 to 1.0 exhibit

larger temperature fluctuation amplitudes, whereas other positions demonstrate relatively smaller amplitudes. The trend of temperature fluctuations over time varies across varying positions, with some locations showing relatively stable fluctuations and others displaying significant variability. In terms of frequency domain characteristics,  $A^*$  is higher in the low-frequency region, indicating that the temperature fluctuation frequencies at most positions are primarily concentrated within the low-frequency range, especially at frequencies less than 10Hz. In the high-frequency region, although the amplitudes at most positions are small, there are still a few notable  $A^*$  values at certain specific positions (such as  $x^*=1.0$  and  $x^*=1.8$ ), indicating the presence of higher temperature fluctuation frequencies at these locations.

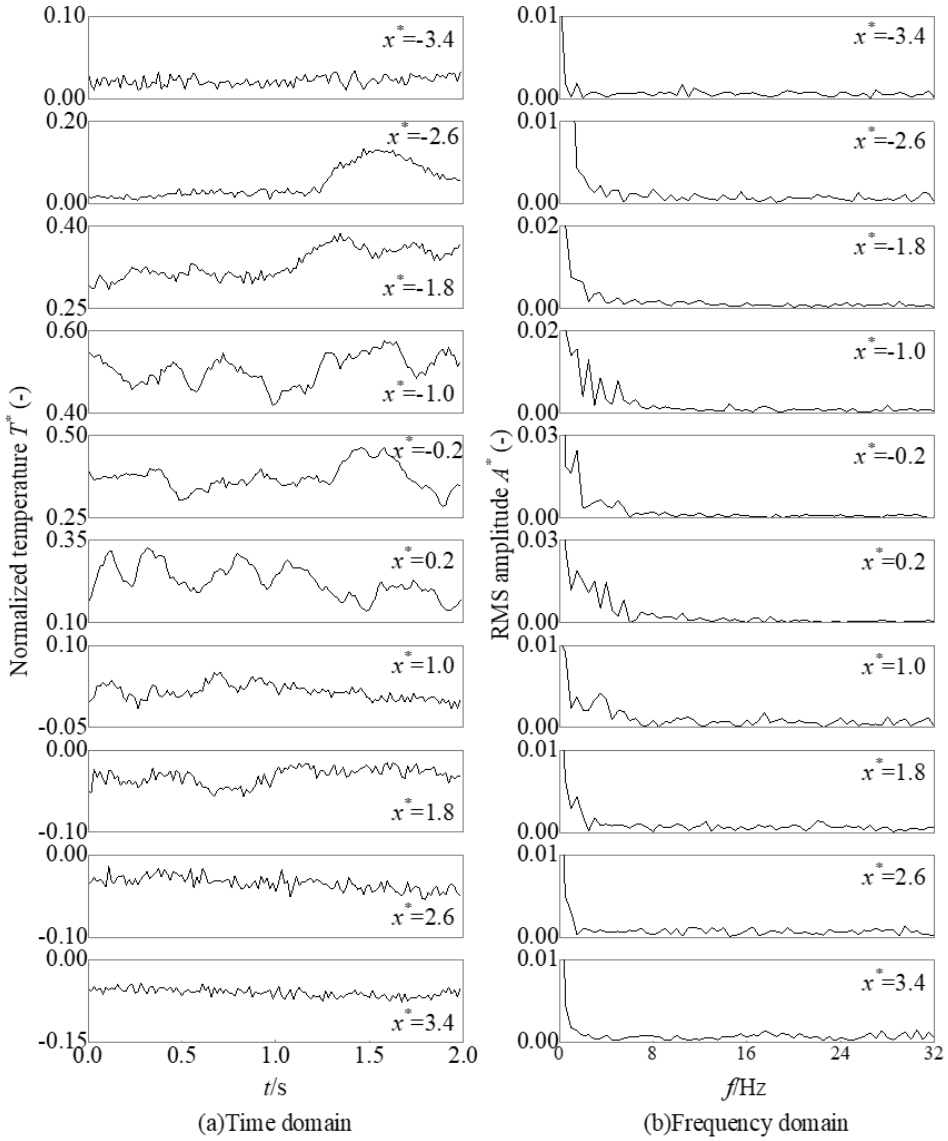


Fig. 12. Normalized temperature and RMS amplitude frequency at  $z^*=6.4$

Fig. 13(a) presents the time-domain profiles of temperature fluctuations of Case 1 at various positions along the  $z$ -axis at  $x^*=-0.2$ , where significant velocity fluctuations

are observed (Fig. 6). Fig. 13(b) displays the corresponding frequency-domain spectra. In the time domain, distinct temporal behaviors of temperature fluctuations are observed at different vertical positions where  $x^*=-0.2$ . At low  $z^*$  values (e.g.,  $z^*=0$ ), the temperature fluctuations are characterized by minimal temporal variation and small oscillation amplitudes. As  $z^*$  increases, the amplitude of temperature fluctuations progressively enlarges. Notably, within the range of 6.4 to 15.9, the fluctuations are more pronounced, exhibiting larger amplitudes. However, further increase in  $z^*$  to 19.1 results in a decrease in amplitude. In the frequency domain, the overall spectral content remains within a range of approximately 10 Hz. The spectral characteristics of temperature fluctuations vary across different positions at  $x^*=-0.2$ . At low  $z^*$  values (e.g.,  $z^*=0$ ), the spectrum remains relatively stable, with uniform frequency components. As  $z^*$  increases, the spectrum becomes increasingly complex, exhibiting a rise in high-frequency components, indicative of a broader distribution of temperature fluctuations across frequencies. Particularly at  $z^*=12.8$  and  $z^*=15.9$ , the spectra displays more pronounced peaks, indicating significant energy concentration at specific frequencies at these positions.

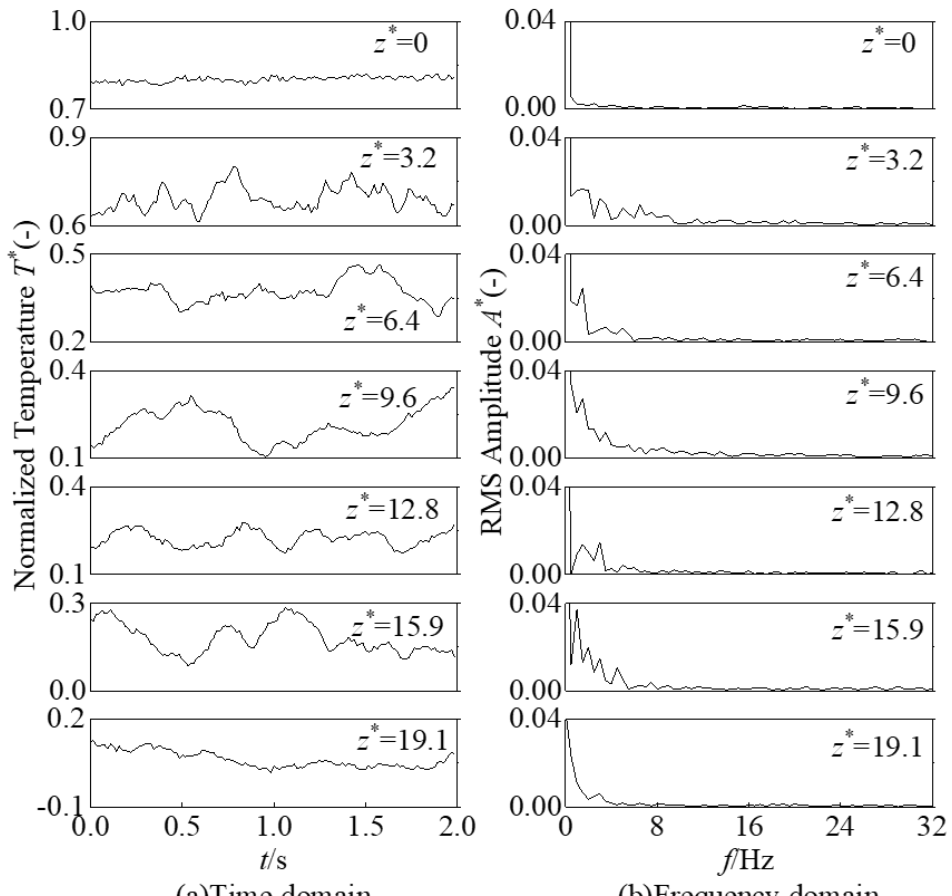


Fig. 13. Normalized temperature and frequency spectrum at  $x^*=-0.2$

Fig. 14 presents the images of the datasets of Case 1 from the same time period as Figs. 13 and 14, after undergoing averaging and normalization processes. Specifically, Fig. 14(a) illustrates the spatial distribution of the average temperature

$(T_{\text{avg}})$  within the mixing zone. Influenced by the initial temperature of the water in the test tank, which is 25°C (below  $T_c$ ), the vertical average temperature starts with a maximum temperature difference of approximately  $\Delta T \approx 10\text{K}$  at the lowest position ( $z^* = 0$ ) and diminishes to around  $\Delta T = 4\text{K}$  in the region within the range of  $z^* = 12$  to 14, maintaining this temperature difference thereafter. Fig. 14(b) displays the normalized average temperature ( $T_{\text{avg}}^*$ ) distribution, offering a clearer visualization of the temperature gradient distribution in both vertical and  $x$ -axis directions.

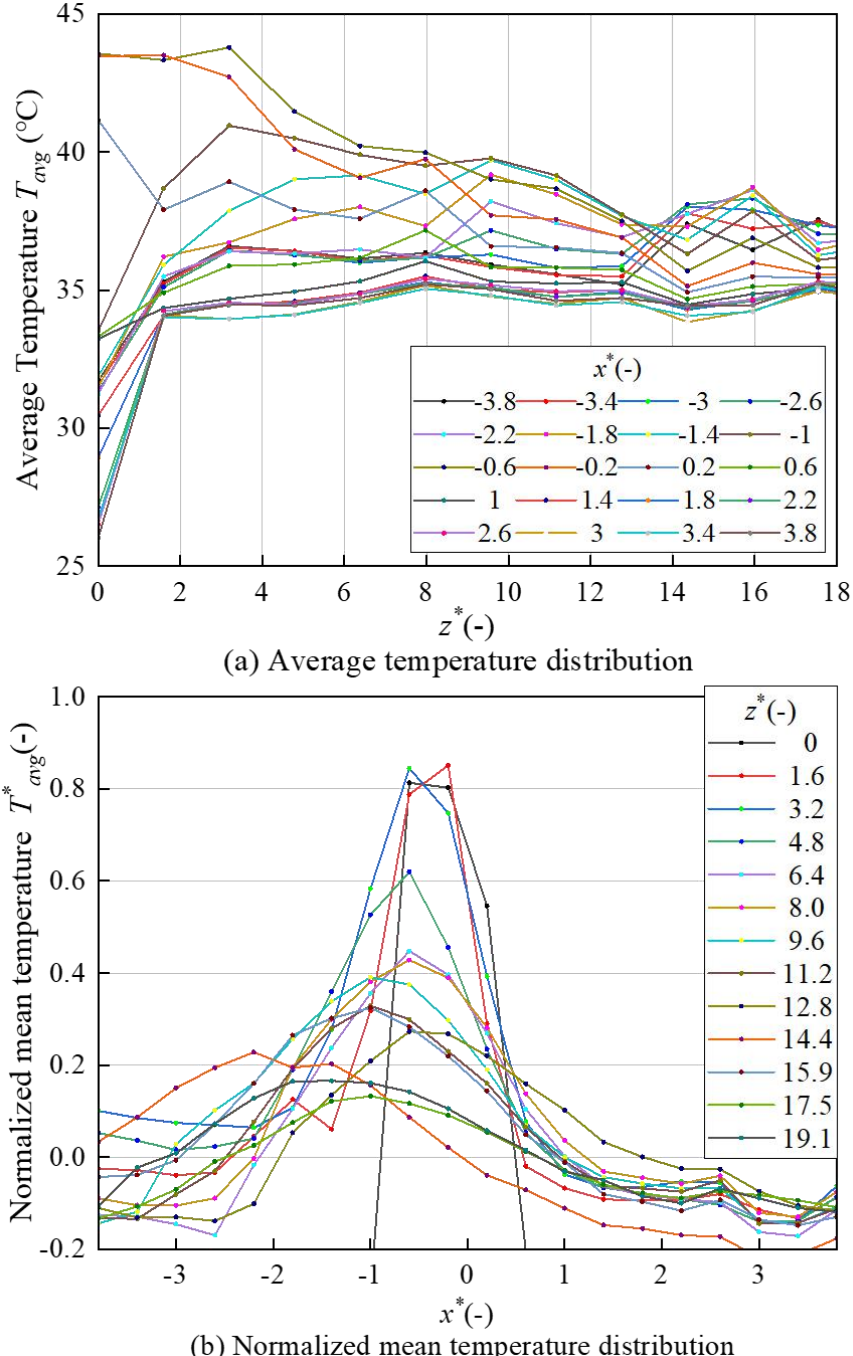


Fig. 14. Average temperature and normalized temperature distribution

The aforementioned conclusions regarding the temperature field were all derived

under the specific conditions outlined in Case 1. To elucidate the influence of diverse factors on the characteristics of thermal mixing temperature fluctuations, the boundary conditions were varied systematically. Specifically, we altered the velocity, temperature, velocity ratio, and inlet hydraulic diameter to obtain temperature data under different conditions for subsequent analysis.

Under conditions of equal initial velocities in both the cold and hot jets, a comparative analysis was conducted to examine the  $T^*_{\text{RMS}}$  variation along the  $z$ -axis at inlet velocities of 1.0 m/s and 1.5 m/s, as shown in Fig. 15. In terms of the vertical distribution of temperature fluctuations, at  $v_c=v_h=1.0$  m/s, the temperature fluctuation intensity at  $z^*=22.3$  is greater than that observed in the range of  $z^*=6.4$  to  $z^*=19.1$ . In contrast, at  $v_c=v_h=1.5$  m, the regions with higher temperature fluctuation intensity are concentrated within  $z^*=6.4$  to  $z^*=12.8$ . These observations clearly indicate that, as the inlet velocity increases, the region of intense thermal mixing does not shift upward. Instead, the height of the region where mixing is most vigorous decreases, suggesting that higher inlet velocities lead to a downward shift of the thermal mixing zone and earlier completion of the mixing process. Furthermore, compared to Fig. 15(a), the maximum normalized root mean square value in Fig. 15(b) is smaller. This observation, when combined with the velocity fluctuation distribution shown in Fig. 8, suggests that as turbulence intensifies (i.e., with increased velocity fluctuations), thermal mixing becomes more effective, leading to a quicker equilibration of local temperature differences. Consequently, the temperature fluctuations are relatively reduced.

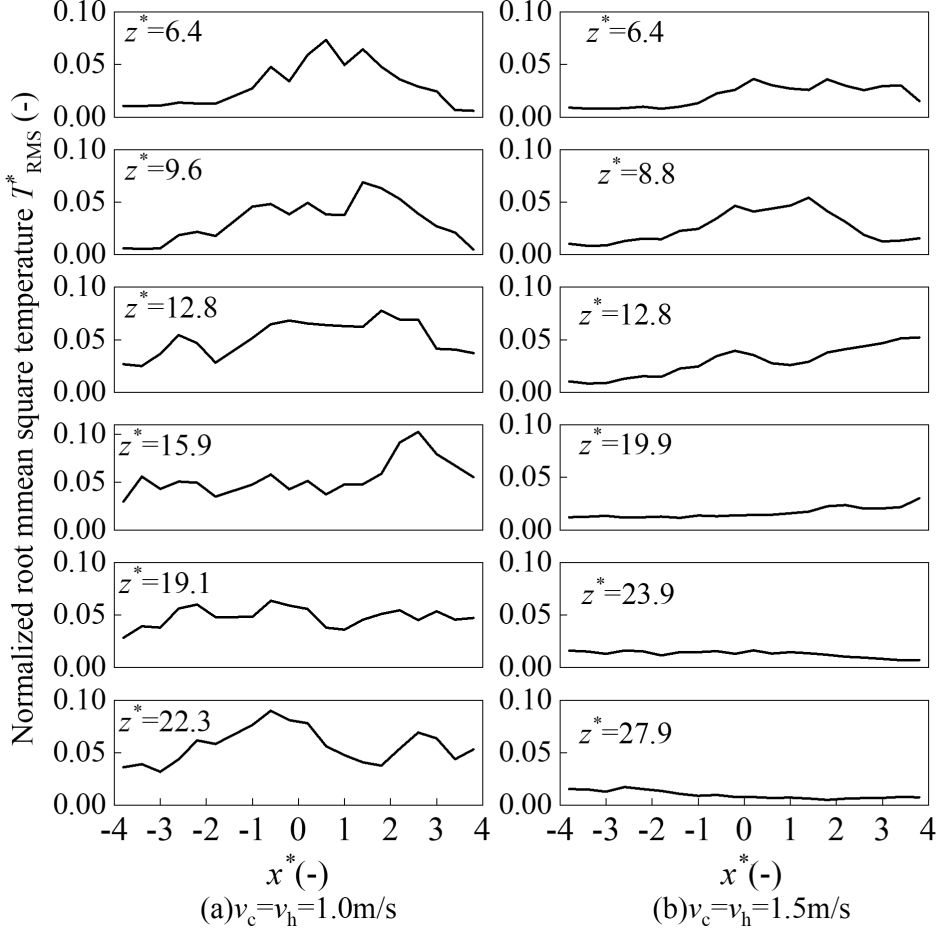


Fig. 15. Normalized RMS temperature under varying inlet velocities ( $v_c = v_h$ )

The relationship between velocity and temperature fluctuations in the mixing zone reveals a clear coupling influenced by the inlet velocity. As observed in Fig. 8 and Fig. 15, higher inlet velocities not only intensify velocity fluctuations but also significantly alter the vertical extent of both velocity and temperature fluctuation regions. For example, at  $v_c=v_h=1.5$  m/s, the peak velocity fluctuations occur at  $z^*=11.2$ , significantly lower than the peaks observed at  $z^*>19$  for lower inlet velocities ( $v_c=v_h=0.5$  m/s or  $1.0$  m/s).

A similar trend is evident in temperature fluctuations: under  $v_c=v_h=1.5$  m/s, the regions of higher temperature fluctuation intensity are concentrated within  $z^*=6.4$  to  $z^*=12.8$ , whereas at  $v_c=v_h=1.0$  m/s, the temperature fluctuation intensity peaks at  $z^*=22.3$ . These findings suggest that higher inlet velocities enhance turbulence intensity, thereby accelerating the mixing process and compressing the regions of both velocity and temperature fluctuations to lower vertical positions. The alignment of the peak velocity and temperature fluctuation regions at higher velocities highlights the strong coupling between momentum-driven turbulence and thermal mixing. This coupling implies that the redistribution of velocity fluctuations due to increased jet momentum directly facilitates faster thermal diffusion, leading to earlier completion of mixing and a downward shift in the thermal mixing zone.

Fig. 16 compares the  $T^*_{RMS}$  distributions within the mixing zone under  $\Delta T$  values

of 15 K and 20 K. Regardless of the temperature difference, the  $T^*_{\text{RMS}}$  distributions exhibit a similar pattern along the  $x$ -axis. Within the mixing zone ( $z^*<14$ ), temperature fluctuations are pronounced, while regions farther downstream show significantly reduced fluctuations. In the downstream region ( $z^*>17$ ), elevated temperature fluctuation intensity is observed near the left wall. This behavior arises from two primary factors: first, the asymmetry in velocity fluctuations described in Fig. 9, where the hot jet demonstrates higher velocity fluctuation intensity; and second, localized mixing between the high-temperature jet and the surrounding static water in the tank. The increased temperature fluctuations near the wall suggest that the mixing mechanism in this area is influenced by interactions between the jet and the ambient water, rather than being solely driven by turbulence associated with velocity fluctuations.

Also, the relationship between velocity fluctuations and temperature fluctuations within the thermal mixing zone reveals a strong coupling influenced by the inlet temperature difference ( $\Delta T$ ). As described in Fig. 9, higher temperature differences ( $\Delta T = 20$  K) result in amplified  $x$ -axis velocity fluctuations, particularly at central positions within the mixing zone ( $z^*=2.8$  and  $z^*=6.8$ ). This intensification of velocity fluctuations directly contributes to enhanced turbulence, which facilitates more vigorous thermal mixing. Similarly, as shown in Fig. 16, elevated temperature fluctuations ( $T^*_{\text{RMS}}$ ) are observed near the same vertical positions within the mixing zone ( $z^*<14$ ) under higher temperature differences, reflecting the impact of intensified turbulence on thermal diffusion.

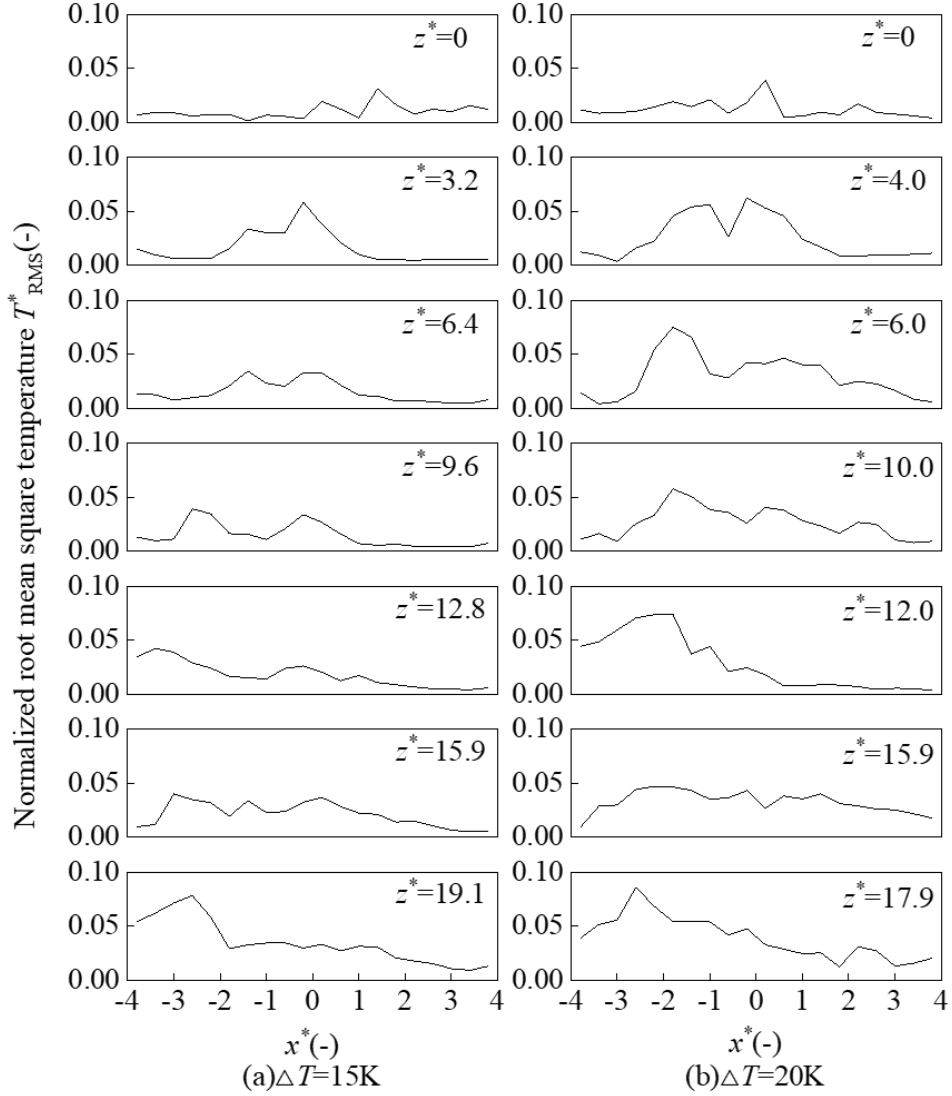


Fig. 16. Normalized RMS temperature under varying temperature difference conditions

Furthermore, after the completion of mixing ( $z^* > 10.8$  in Fig. 9 and  $z^* > 14$  in Fig. 16), asymmetry becomes evident in both velocity and temperature fluctuations. For instance, the pronounced asymmetry in velocity fluctuations at  $z^* = 14.8$  and  $z^* = 16.7$  under  $\Delta T = 20$  K (Fig. 9) aligns with the elevated temperature fluctuations observed near the left wall in Fig. 16. This asymmetry arises from the stronger momentum and mixing effects of the hot jet, as well as its interaction with the surrounding static water.

Fig. 17 shows the  $T^*_{\text{RMS}}$  distributions in the thermal mixing zone under the different velocity ratios. When  $R=1$ , the temperature fluctuation distribution is generally symmetric around the central  $x$ -axis, except for localized regions on the hot jet side, where elevated fluctuations are observed. This is attributed to the hot jet's higher momentum and its interaction with the ambient-temperature water. When  $R=0.5$  or  $R=2$ , the temperature fluctuation distribution becomes asymmetric, consistently favoring the side with the higher inlet velocity. Under varying velocity

ratios, the side with the higher jet velocity exhibits more intense temperature fluctuations. This is due to the enhanced turbulent mixing and shear forces generated on that side, which result in more vigorous interaction between the high-velocity fluid and the surrounding fluid. The intensified mixing leads to greater local temperature variations, as the increased frequency and intensity of these interactions amplify the thermal fluctuations.

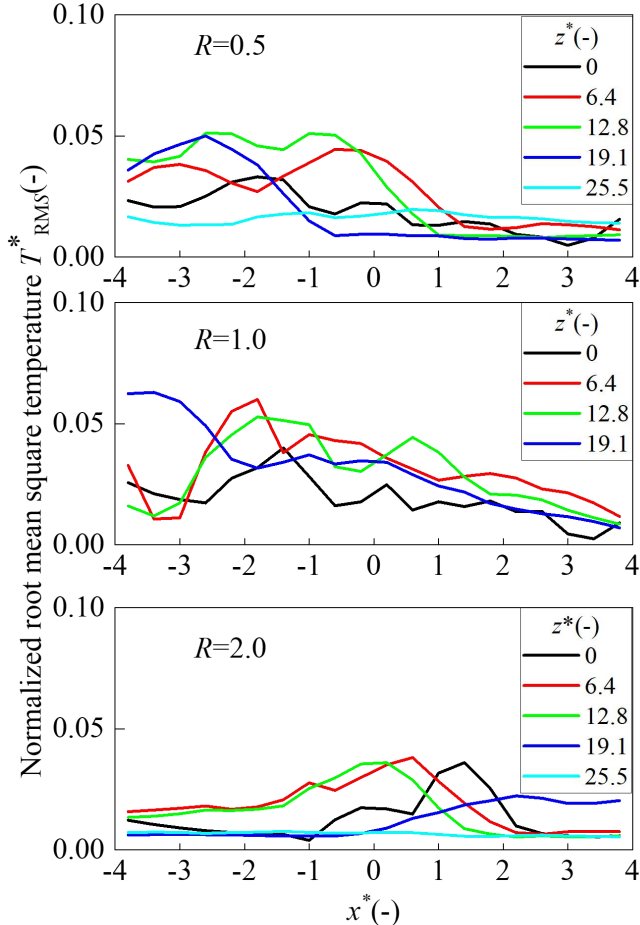


Fig. 17. Normalized RMS temperature under varying velocity ratios

The relationship between velocity and temperature fluctuations under varying velocity ratios ( $R$ ) demonstrates a strong coupling influenced by jet dynamics and turbulent mixing. As shown in Fig. 10, the velocity fluctuation distribution becomes asymmetric when  $R = 0.5$  (faster hot jet) or  $R = 2$  (faster cold jet), with higher Std. Dev. observed on the side of the faster jet. This asymmetry reflects the dominance of the jet with greater momentum, which drives stronger turbulence and improves mixing efficiency. Similarly, Fig. 17 shows a corresponding asymmetry in temperature fluctuations ( $T^*_{RMS}$ ), with elevated fluctuations on the faster jet side. This alignment highlights the role of velocity fluctuations in enhancing turbulence, which accelerates thermal diffusion and amplifies temperature variations due to intensified shear forces and frequent fluid interactions.

Variations in the velocity ratio ( $R$ ) directly influence the spatial distribution and

intensity of both velocity and temperature fluctuations, underscoring the interplay between momentum-driven turbulence and thermal diffusion. The results indicate that efficient thermal mixing is largely governed by the strength and asymmetry of the velocity fluctuations, which drive the rate of thermal energy transfer and ultimately determine the mixing dynamics.

Fig. 18 compares the  $T^*_{\text{RMS}}$  values under different inlet hydraulic diameters of 5.71, 12.54 and 18.59. With increasing  $D^*$ , the intensity of temperature fluctuations in the central region significantly enhances. The peak location of temperature fluctuations shifts to lower  $z^*$  values as  $D^*$  increases:  $z^* = 28$  for  $D^* = 5.71$ ,  $z^* = 12.8$  for  $D^* = 12.54$ , and  $z^* = 4.3$  for  $D^* = 18.59$ . This trend demonstrates that as  $D^*$  grows, the region with the most pronounced temperature fluctuations moves closer to the inlet.

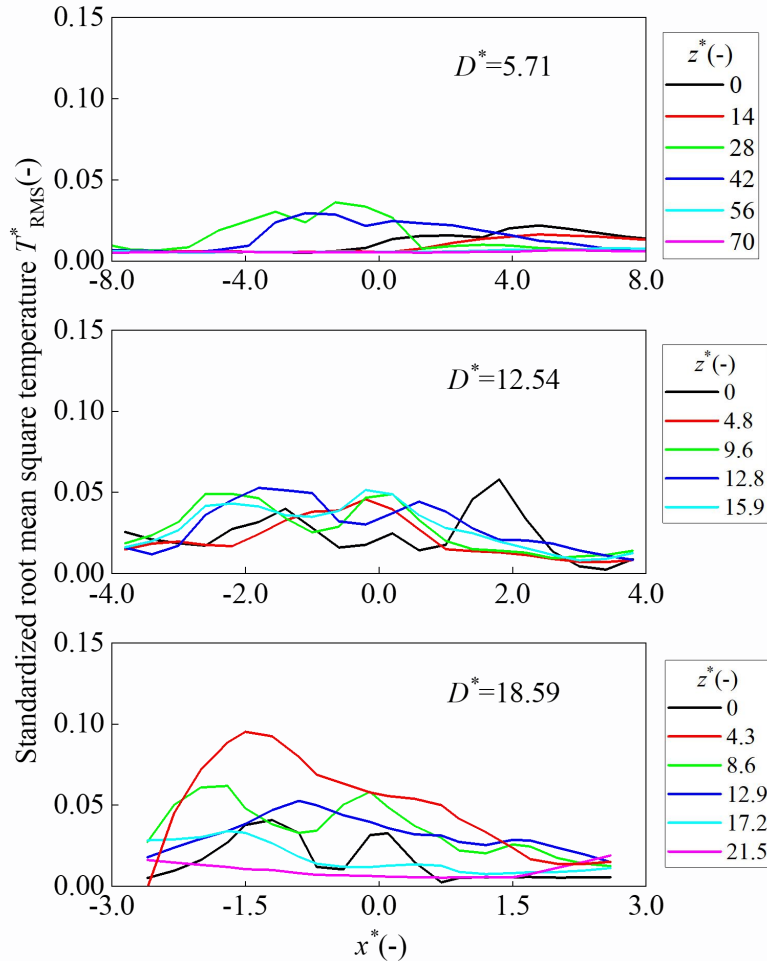


Fig. 18. Normalized RMS temperature under varying inlet hydraulic diameter conditions

The relationship between velocity fluctuations and temperature fluctuations in the thermal mixing zone is strongly coupled and significantly influenced by the inlet hydraulic diameter ( $D^*$ ). As illustrated in Fig. 11, an increase in  $D^*$  (from 5.71 to 18.59) amplifies the peak Std. Dev. of the  $x$ -axis velocity component, indicative of enhanced

turbulent mixing intensity. For smaller diameters ( $D^*=5.71$ ), weaker velocity fluctuations are distributed over a broader downstream region, with peak turbulence occurring farther from the inlet ( $z^*$ ). This spatial separation correlates with delayed and less efficient mixing. Conversely, larger diameters ( $D^* \geq 12.54$ ) generate stronger velocity fluctuations localized near the inlet, accelerating turbulent energy dissipation and promoting rapid, localized mixing.

With increasing  $D^*$ , the  $T^*_{\text{RMS}}$  peaks shift significantly toward the inlet ( $z^*=28 \rightarrow 4.3$ ), accompanied by a notable rise in the intensity of temperature fluctuations. This behavior aligns with the enhanced turbulent kinetic energy associated with larger hydraulic diameters, which promotes more vigorous mixing and heat transfer. The shift in peak locations indicates that larger  $D^*$  values not only intensify velocity fluctuations but also bring the regions of maximum temperature fluctuations closer to the inlet, reducing the characteristic length scale over which mixing occurs. Thus, the hydraulic diameter plays a critical role in governing the spatial and temporal coupling of velocity and temperature fluctuations, with larger diameters fostering concurrent, high-intensity fluctuations that optimize thermal mixing efficiency by aligning the regions of maximum momentum and thermal activity.

## 4. Conclusions

In this study, an experimental investigation on the thermal mixing characteristics of parallel twin water jets was conducted using UDV. The effects of inlet velocity, temperature difference, velocity ratio, and hydraulic diameter were systematically analyzed. The key conclusions are as follows:

### (1) Flow field characteristics

Thermal mixing predominantly occurs within a confined rectangular zone near the jet inlets (Fig. 4), characterized by intense turbulence with recirculation phenomena (Figs. 5-7). Transient velocity fluctuations in the  $x$ -axis exhibit symmetric distributions (Fig. 7b), and their intensity scales with inlet velocity (Fig. 8). These observations align with the UDV-measured velocity profiles and turbulence statistics.

### (2) Temperature field characteristics

Temperature fluctuations exhibit significant spatial variations along both  $x$ - and  $z$ -axes (Figs. 12-14), with dominant frequencies below 10 Hz (Fig. 12b). The  $T^*_{\text{RMS}}$  peaks within the mixing zone ( $z^* < 14$ ) and diminishes downstream (Fig. 14), confirming localized thermal mixing followed by stabilized temperature distributions.

### (3) Impact of inlet condition

**Velocity and temperature difference:** Increased inlet velocity (Figs. 8, 15) and temperature difference (Figs. 9, 16) enhance turbulence intensity, accelerating thermal diffusion and compressing the mixing region vertically.

**Velocity ratio asymmetry:** Velocity ratios  $R \neq 1$  induce asymmetric velocity (Fig. 10) and temperature fluctuations (Fig. 17), with higher turbulence intensity on the faster jet side due to momentum dominance.

**Hydraulic diameter:** Larger diameters ( $D^* \geq 12.54$  mm) intensify velocity fluctuations near the inlet (Fig. 11) and shift temperature fluctuation peaks closer to the jet source (Fig. 18), indicating enhanced mixing efficiency.

#### (4) Velocity-temperature coupling

Velocity fluctuations directly govern turbulence intensity, which amplifies thermal diffusion (Figs. 8 vs. 15, 9 vs. 16). Regions of high velocity pulsations (e.g.,  $z^* \approx 11.2$  for  $v=1.5\text{m/s}$ ) coincide with elevated  $T^*_{\text{RMS}}$  values, demonstrating a spatiotemporal coupling between momentum and thermal fields.

This study validates the applicability of UDV for transient velocity measurements in jet mixing, providing critical insights for subsequent lead-bismuth experiments. The experimental database supports future numerical simulations and safety analyses of Lead-cooled Fast Reactors (LFRs).

## Acknowledgments

This work was supported and funded by the Fundamental Research Funds for the Central Universities (No. 3072024CFJ1506).

## References

- [1] Ohshima, H., Muramatsu, T., Kobayashi, J., et al., 1994. Current status of studies on temperature fluctuation phenomena in LMFRRs. In: IAEA/IWGFR Specialist Meeting on Correlation between Material Properties and Thermohydraulics Conditions in Liquid Metal-cooled Fast Reactors (LMFRs), Aix-en-Provence, France, 22-24 November.
- [2] Choi, S.K., Han, J.W., Kim, D., et al., 2015. The present state-of-the-art thermal striping studies for sodium-cooled fast reactors. In: Proceedings of the 16th International Topical Meeting on Nuclear Reactor Thermal Hydraulics (NURETH-16), Chicago, USA, August 30-September 4, pp. 6614-6624.
- [3] Brunings, J.E., 1982. LMFBR Thermal-Striping Evaluation. Electric Power Research Institute, Report No. EPRI-NP-2672.
- [4] Chellapandi, P., Chetal, S.C., Raj, B., 2009. Thermal striping limits for components of sodium-cooled fast spectrum reactors. Nucl. Eng. Des. 239 (12), 2754-2765.
- [5] Tenchine, D., 2010. Some thermal hydraulic challenges in sodium cooled fast reactors. Nucl. Eng. Des. 240 (5), 1195-1217.
- [6] Moriya, S., Ohshima, I., 1990. Hydraulic similarity in the temperature fluctuation phenomena of non-isothermal coaxial jets. Nucl. Eng. Des. 120 (2-3), 385-393.
- [7] Tenchine, D., Moro, J.P., 1997. Experimental and numerical study of coaxial jets. In: Proceedings of the 8th International Topical Meeting on Nuclear Reactor Thermal-Hydraulics (NURETH-8), Kyoto, Japan, pp. 1381-1387.
- [8] Ahmed, M.R., Sharma, S.D., 2000. Effect of velocity ratio on the turbulent mixing of confined, co-axial jets. Exp. Therm. Fluid Sci. 22 (1-2), 19-33.
- [9] Wakamatsu, M., Nei, H., Hashiguchi, K., 1995. Attenuation of temperature fluctuations in thermal striping. J. Nucl. Sci. Technol. 32 (8), 752-762.
- [10] Tokuhiro, A., Kimura, N., 1999. An experimental investigation on thermal striping: mixing phenomena of a vertical non-buoyant jet with two adjacent buoyant

jets as measured by ultrasound Doppler velocimetry. *Nucl. Eng. Des.* 188 (1), 43-73.

[11] Kimura, N., Miyakoshi, H., Kamide, H., 2007. Experimental investigation on transfer characteristics of temperature fluctuation from liquid sodium to wall in parallel triple-jet. *Int. J. Heat Mass Transf.* 50 (9-10), 2024-2036.

[12] Lu, D., Cao, Q., Lv, J., et al., 2012. Experimental study on three-dimensional temperature fluctuation caused by coaxial-jet flows. *Nucl. Eng. Des.* 242, 234-242.

[13] Cao, Q., Li, H., Lu, D., et al., 2017. Temperature fluctuation caused by coaxial-jet flow: experiments on the effect of the velocity ratio  $R \geq 1$ . *Nucl. Eng. Des.* 314, 142-149.

[14] Kok, B., Varol, Y., Ayhan, H., et al., 2017. Experimental and computational analysis of thermal mixing characteristics of a coaxial jet. *Exp. Therm. Fluid Sci.* 82, 276-286.

[15] Kok, B., Varol, Y., Ayhan, H., et al., 2020. Experimental and LES simulation of thermal mixing behavior of a twin-jet flow with sequential cylindrical obstacles. *Int. Commun. Heat Mass Transf.* 114, 104576.

[16] Roelofs, F., 2020. Liquid metal thermal hydraulics: state-of-the-art and future perspectives. *Nucl. Eng. Des.* 362, 110590.

[17] Yu, Y.Q., Merzari, M., Thomas, J.W., et al., 2017. Steady and unsteady calculations on thermal striping phenomena in triple-parallel jet. *Nucl. Eng. Des.* 312, 429-437.

[18] Tenchine, D., Vandroux, S., Barthel, V., et al., 2013. Experimental and numerical studies on mixing jets for sodium-cooled fast reactors. *Nucl. Eng. Des.* 263, 263-274.

[19] Chacko, S., Chung, Y.M., Choi, S.K., et al., 2011. Large-eddy simulation of thermal striping in unsteady non-isothermal triple jet. *Int. J. Heat Mass Transf.* 54 (19-20), 4400-4409.

[20] Angeli, P.E., 2019. Verification and validation of LES of a triple parallel jet flow in the context of a thermal striping investigation. *Nucl. Eng. Des.* 353, 110210.

[21] Cao, Q., Liu, S., Lu, D., et al., 2018. Numerical study on temperature fluctuation of upper plenum in FBR with a more realistic model. *Ann. Nucl. Energy* 114, 214-226.

[22] Wang, Y., Wang, M., Zhang, J., et al., 2021. Large eddy simulation on the mixing characteristics of liquid sodium at the core outlet of sodium-cooled fast reactors (SFR). *Ann. Nucl. Energy* 159, 108347.

[23] Jung, Y., Choi, S.R., Hong, J., 2022. Numerical analysis of temperature fluctuation characteristics associated with thermal striping phenomena in the PGSFR. *Nucl. Eng. Technol.* 54 (10), 3928-3942.

## Nomenclature

### Abbreviations

RMS	Root-mean-square
Std. Dev.	Standard deviation
LMFR	Liquid metal fast reactor
URANS	Unsteady Reynolds-averaged Navier-stokes
LES	Large eddy simulation
UDV	Ultrasonic Doppler Velocimetry
PIV	Particle image velocimetry
LFRs	Lead-cooled Fast Reactors

### Symbols

$x$	$X$ -axis position (mm)
$z$	Vertical position (mm)
$d$	Width of inlet nozzles
$x^*$	Normalized $x$ -axis position
$z^*$	Normalized vertical position
$v$	Velocity (m/s)
$v_x$	Velocity component in the $x$ -direction
$\bar{v}$	Average velocity
$\sigma_x$	Standard deviation of velocity
$t$	Time (s)
$T$	Fluid temperature (°C)
$T_c$	Inlet cold fluid temperature (°C)
$T_h$	Inlet hot fluid temperature (°C)
$\Delta T$	Inlet cold and hot temperature difference (°C/K)

$T_{\text{avg}}$	Average temperature (°C)
$T^*$	Normalized temperature
$T^*_{\text{RMS}}$	Normalized root-mean-square temperature
$D^*$	The hydraulic diameter of inlet nozzles